Stability of Pt10Sn3 Clusters Supported on γ–Al2O3 in Oxidizing Environment : a DFT Comparison of Alloying and Size Effects

Masoud Shahrokhi, Céline Chizallet, David Loffreda, Pascal Raybaud

ChemCatChem

Research Article
doi.org/10.1002/cctc.202201089

Chemistry Europe
European Chemical Societies Publishing

www.chemcatchem.org

Special Collection

Stability of $Pt_{10}Sn_3$ Clusters Supported on γ-Al_2O_3 in Oxidizing Environment: a DFT Comparison of Alloying and Size Effects

Masoud Shahrokhi,[a, b] Celine Chizallet,[a] David Loffreda,[b] and Pascal Raybaud*[a, b]

The understanding of the structure and properties of γ-Al_2O_3 supported platinum-tin catalysts in oxidizing conditions is of prominent importance for many catalytic reactions. By using density functional theory calculations and ab initio molecular dynamics simulations, we identify the adsorption sites of oxygen atoms on a $Pt_{10}Sn_3$/γ-Al_2O_3(100) cluster model and analyze its reconstruction and electronic charge redistribution. A strengthening of O adsorption is found for the cluster with respect to the Pt_3Sn(111) surface, due to the key role of Al–Pt interfacial sites at low coverage, the ductility and the metastability of the cluster. Moreover, the ab initio (p_{O_2}, T) thermodynamic phase diagrams show only minor differences between the supported $Pt_{10}Sn_3$ and Pt_{13} clusters. Both clusters are much more oxidized than their homologous Pt and Pt_3Sn-(111) surfaces, and their oxygen contents may exceed 1 ML. This suggests a stronger size effect than an alloying effect for the oxidation of the metallic PtSn nanoparticles at small size.

Introduction

Supported platinum-based (Pt-based) particles have a great potential at sub-nanometric size, mainly for catalytic applications. For instance, Pt clusters supported on γ-alumina are well known to be active catalysts used in numerous applications such as naphtha reforming catalytic processes,[1,2] light alkane dehydrogenation and cyclohexane dehydrogenation for hydrogen production.[3,4] γ-alumina supported Pt catalysts are also widely used for the oxidation reactions of various molecules such as hydrocarbons (methane, propane,…)[5] as well as carbon monoxide (CO).[6,7] This type of catalytic material is also well-known to be efficient for O_2 reduction reaction (ORR)[8] which is of renewed interest nowadays within the context of hydrogen purification.[9] Nevertheless, one open question remains about the oxidation state of platinum in oxidizing conditions. In particular, it has been reported by *in situ* XAS experiment that such alumina supported Pt may become partially oxidized upon oxygen environment encountered in CO oxidation reaction,[10] while density functional theory (DFT) calculations also showed that the oxidizability of Pt is increased for small size clusters.[11,12]

The performance of Pt-based catalysts can be improved by modifying their properties with a secondary metallic promoter.[13–17] These promoters may improve the activity, the selectivity, and the stability of the resulting Pt-based nanoalloy catalysts by either modifying the electronic properties ("electronic effect") or diluting the main active metal ("geometric effect").[18] Tin (Sn) is a typical example that can increase the catalytic performance of Pt by forming Pt–Sn alloy. Sn doped Pt-based particles are widely used to improve the selectivity, stability and regeneration properties in many catalytic applications such as dehydrogenation of alkanes and catalytic reforming of naphtha.[19–21] The addition of Sn is especially observed to weaken propene adsorption[22] and to improve the selectivity of dehydrogenation of propane on Pt catalyst,[15] or to avoid the coking.[16] Moreover, tin is a good choice to alloy with Pt for yielding higher catalytic activity as a cathodic electrocatalyst[23] for various applications such as oxidation reactions or oxygen reduction reaction (ORR).[14,24–28] The redox active Sn ad-atoms were found to highly promote the CO adlayer oxidation on Pt.[27] Theoretical studies showed that the catalytic performance of Pt can be enhanced in different catalytic reactions by forming Pt–Sn alloy.[29–31] By performing density functional theory (DFT) calculations in periodic boundary conditions, Wang *et al.* showed that at the same temperature, the rate of ORR on the Pt_3Sn(111) surface is faster than that on the pure Pt(111) surface. This was assigned to a decrease in the surface *d*-band center of Pt_3Sn(111) in comparison to pure Pt(111), that leads to a corresponding decrease in the binding energies of ORR intermediates.[30] Regarding low dimensionality alloyed systems, the effects of

[a] *Dr. M. Shahrokhi, Dr. C. Chizallet, Dr. P. Raybaud*
IFP Energies nouvelles
Rond-point de l'échangeur de Solaize
BP 3
69360 Solaize (France)
E-mail: pascal.raybaud@ifpen.fr
Homepage: https://www.ifpenergiesnouvelles.com/page/pascal-raybaud
[b] *Dr. M. Shahrokhi, Dr. D. Loffreda, Dr. P. Raybaud*
ENSL, CNRS, Laboratoire de Chimie UMR 5182
46 Allée d'Italie
69364 Lyon (France)

Supporting information for this article is available on the WWW under https://doi.org/10.1002/cctc.202201089

This publication is part of a Special Collection on "French Conference on Catalysis 2022". Please check the ChemCatChem homepage for more articles in the collection.

cluster size and composition on the atomic structures, electronic and chemical bonding properties of Pt_nSn_n (n = 1—10) and $Pt_{3m}Sn_m$ (m = 1—5) were determined by combining genetic algorithms with DFT by Huang *et al.*.[31] Both charge transfer (from Sn to Pt) and dilution effect of Pt sites seem to act beneficially for improving the catalytic activity of Pt–Sn catalysts.[31]

Γ-Al_2O_3 is a very widely used support in heterogeneous catalysis and in industrial processes because of its high surface area, versatile acid-basic properties and ability to disperse the metallic active phase.[32] In particular, Pt and Pt–Sn clusters with nanometric sizes could be dispersed at the surface of Al_2O_3 support.[1,28,33] Gorczyca *et al.* reported a DFT investigation of structural models for platinum-tin sub-nanometric clusters, containing thirteen metal atoms (Pt_xSn_{13-x} with $0 \leq x \leq 13$) deposited on the (100) γ-Al_2O_3 surface.[19] Previous experimental works suggest that a lower amount of tin with respect to platinum is present in the reduced nano-alloy,[1,21,34] therefore Gorczyca *et al.* studied especially the nanostructure of $Pt_{10}Sn_3$ on γ-Al_2O_3 and the effects of hydrogen adsorption on the metallic cluster, so as to assess the evolution of the morphology of the cluster and of its electronic properties in a reducing environment. A dual effect of dilution and ductility of the sub-nanometric cluster, enhanced by the presence of tin, explained its behavior as a function of the hydrogen coverage. To date, however, no theoretical work has addressed the interaction with O_2 of platinum-tin clusters on alumina. As highlighted above, the behavior of such alloyed clusters in oxidative conditions is critical for the evolution of catalytic performances in presence of O_2. Previous theoretical works revealed that the reactivity of O_2 with Cu clusters is structure-sensitive while the thermodynamic stability and activation energies depend on cluster's size and morphology.[35] However, to the best of our knowledge, the thermodynamic stability and the nanostructure evolution of PtSn alloyed cluster under various O_2 partial pressures remain unknown.

To address such a question, the present work reports on the dissociative adsorption of oxygen $Pt_{10}Sn_3$/γ-Al_2O_3 catalysts over a large range of coverage by performing density functional theory calculations and ab initio molecular dynamics (AIMD) simulations. The stability of the cluster and its O coverage is predicted by atomistic thermodynamics for $Pt_{10}Sn_3O_n$/γ-Al_2O_3 (100) as a function of O_2 pressure and temperature. To elucidate the effect of alloying and size, the results are compared with oxygen adsorption on Pt_{13}/γ-Al_2O_3, Pt(111) and Pt_3Sn(111) extended surfaces. We discuss the trends by analyzing the evolution of structure, adsorption energy, Bader charge transfer and thermodynamic stability as a function of oxygen coverage.

Results and discussion

Adsorption of atomic oxygen at low coverage

In this section, we first discuss the adsorption of a single oxygen atom on $Pt_{10}Sn_3O/Al_2O_3$. Due to the absence of symmetry, there exists a variety of possible adsorption sites for O on the $Pt_{10}Sn_3$ cluster. First, we simulated all typical adsorption sites for oxygen (top, bridge, and hollow sites) as initial guesses. Among all the simulated configurations, only the most stable ones are shown in Figure 1 and their adsorption energies are given in Table 1.

The O adsorption energy on the Pt top site (−182 kJ.mol^{-1}) with a Pt–O bond length of 1.79 Å is twice stronger than that on the Sn top site (−85 kJ.mol^{-1}) with a Sn–O bond length of 1.87 Å. This result which does not follow the intuitive expectation based on electronegativity of Pt and Sn elements, highlights that the specific behavior of such nano-cluster is driven in particular by the low coordination of Pt atoms. Also, the bimetallic hollow (Pt–Sn–Pt) site with an adsorption energy of −48 kJ.mol^{-1} site is the least stable structure which is in contrast with the Pt_3Sn(111) surface as discussed below. However, the bimetallic bridge (Al–Pt) interfacial site is by far the most stable position with an adsorption energy of −390 kJ.mol^{-1}. The same mode is favored on the Pt_{13}/Al_2O_3 system.[12] In this most stable configuration, the Pt–O and Al–O bond lengths are 1.89 and 1.83 Å, respectively. As illustrated for some configurations in Table 1, the O adsorption energies on $Pt_{10}Sn_3/Al_2O_3$ in all configurations are significantly less exothermic than those on Pt_{13}/Al_2O_3.[12] The adsorption energy for the most stable configuration at interfacial site on $Pt_{10}Sn_3/Al_2O_3$ is more exothermic (ie. stronger adsorption) than those found on extended monometallic Pt(111),[36–38] and bimetallic Pt_3Sn-(111)[24,25] surfaces at 0.25 ML O coverage (for which we also

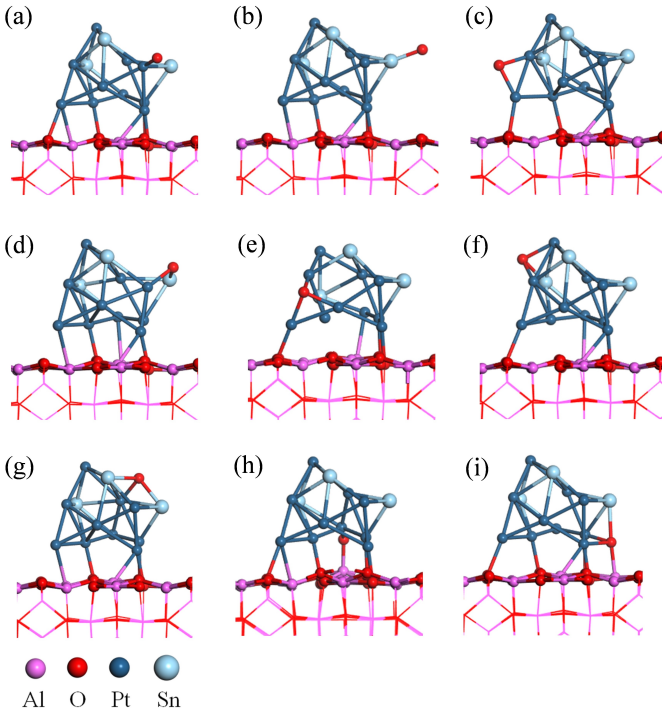

Figure 1. Side views of the most stable structures for an atomic oxygen adsorption on $Pt_{10}Sn_3$/γ-Al_2O_3 system in different positions: (a) top-Pt, (b) top-Sn, (c) bridge (Pt–Pt), (d) bimetallic bridge (Pt–Sn), (e) hollow (Pt–Pt–Pt), (f) bimetallic hollow (Pt–Sn–Pt), (g) bimetallic hollow (Sn–Pt-Sn), (h) interfacial (with alumina) bimetallic bridge (Al–Pt) and (i) interfacial (with alumina) trimetallic hollow (Al–Pt–Sn).

Table 1. Adsorption energy (E_{ads}, in kJ/mol) per O_2 at low oxygen coverage for the most stable structures. The related structures are presented in Figure 1. The reported adsorption energies in Ref. [24] are per atomic oxygen, therefore they are multiplied by two in this work.

System	Adsorption mode	Figure	E_{ads}
$Pt_{10}Sn_3O_1/Al_2O_3$ this work	Top-Pt	Figure 1 (a)	−182
	Top-Sn	Figure 1 (b)	−85
	Bridge (Pt-Pt)	Figure 1 (c)	−203
	Bimetallic bridge (Pt-Sn)	Figure 1 (d)	−250
	Hollow (Pt-Pt-Pt)	Figure 1 (e)	−209
	Bimetallic hollow (Pt-Sn-Pt)	Figure 1 (f)	−48
	Bimetallic hollow (Sn-Pt-Sn)	Figure 1 (g)	−250
	Bimetallic bridge (Al-Pt)	Figure 1 (h)	−393
	Trimetallic hollow (Al-Pt-Sn)	Figure 1 (i)	−274
$Pt_{13}O_1/Al_2O_3$[12]	Top-Pt		−376
	Bridge (Pt-Pt)		−351
	Hollow (Pt-Pt-Pt)		−367
	Bimetallic bridge (Al-Pt)		−452
	Bimetallic hollow (Al-2Pt)		−514
Pt(111)–(2×2) this work	0.25 ML	Figure S4	−244
Pt (111)–(2×2)[36,37]	0.25 ML		−233 and −199
Pt (111)–(2√3×2√3)[38]	1/12 ML		−236
Pt_3Sn (111)–(2√3×4) this work	0.25 ML	Figure S5	−209
Pt_3Sn (111)–(2×2)[39]	0.25 ML		−204
Pt_3Sn (111)–(2×2)[24]	0.25 ML		−216
Pt_3Sn (111))–(√3×√3)R30°[24]	0.25 ML		−199

provide a value compatible with previous works) (Table 1). The adsorption energy on alloyed $Pt_3Sn(111)$ surface is −209 kJ/mol at 0.25 ML O coverage in our study (Figure S5) which is in good agreement with previous work (−204 kJ/mol).[39] This adsorption which occurs on a bimetallic hollow (Pt–Sn–Pt) site of the $Pt_3Sn(111)$ surface is more exothermic than the adsorption occurring on the homologous site of $Pt_{10}Sn_3/Al_2O_3$ (−48 kJ/mol) but less exothermic than the most stable interfacial (Al–Pt–Sn) site on $Pt_{10}Sn_3/Al_2O_3$.

Oxygen adsorption at higher coverages

To identify stable configurations of higher oxygen coverages on $Pt_{10}Sn_3/Al_2O_3$, AIMD simulations were used systematically from $Pt_{10}Sn_3O_2$ to $Pt_{10}Sn_3O_{30}$ (Figure S2), as explained in the computational details. The structures of the most stable $Pt_{10}Sn_3O_n/\gamma$-Al_2O_3 systems are displayed in Figure S3. To make a parallel analysis with infinite surface, for each oxygen coverage, the monolayer is defined as the number of oxygen atoms normalized by 13, the total number of metallic atoms in the ductile cluster. Therefore, the 26 atomic oxygen coverage ($Pt_{10}Sn_3O_{26}$) is considered as a 2 ML structure. On $Pt_{10}Sn_3O_2$, the two adsorbed oxygen atoms are linked at the interface of the cluster and the alumina support through bimetallic bridge (Pt–Al) and trimetallic hollow (Al–Pt–Sn) configurations. From $n > 4$, the cluster is gradually reconstructed with the uplift of the platinum-tin cluster. This reconstruction induced by oxygen insertion between metallic atoms results in a cluster's volume expansion. For $n = 4$, in addition to the interfacial oxygen atoms, the bridge (Pt–Pt) and bimetallic bridge (Pt–Sn) adsorption modes are also occupied by O atoms on the cluster, while for $n > 6$ in addition to the interfacial oxygen atoms, the bridge (Pt–Pt, Pt–Sn and Sn–Sn) and bimetallic hollow sites are favored. From $n = 4$ to $n = 10$, oxygen atoms are adsorbed only on the outer layer of metallic cluster whereas for higher O coverages ($n > 10$) they penetrate the center of cluster. For the structures at very high coverages ($n = 22$, 24 and 26), one short O–O bond (between 1.37 and 1.41 Å) is formed with the O-O species connecting two Pt atoms on the outer layer of the cluster. For $n = 28$, in addition to this outer layer O–O bond, a second O–O bond (1.33 Å) is located in the center of metallic cluster (bridging two Pt atoms), while a third one (1.34 Å) is formed at the interface between one Pt and one Al, for $n = 30$. Finally, for the structure of highest oxygen coverage ($n = 30$) additional oxygen atoms are adsorbed in the top-Sn mode (Figure S3).

The energetic feature of the most stable $Pt_{10}Sn_3O_n/\gamma$-Al_2O_3 systems found is shown in Figure 2. The average adsorption energy increases from −393 kJ/mol (for $Pt_{10}Sn_3O$) to −145 kJ/mol (for $Pt_{10}Sn_3O_{30}$) in a quasi-monotonous way as a function of O coverage due to several effects induced by the different nature of sites involved in the interaction with O (interfacial, Pt, Sn) and to the repulsion between adsorbates particularly at high coverage. The exothermicity of O adsorption first decreases from −393 kJ/mol (for $n = 1$) to −286 kJ/mol (for $n = 4$) and then reaches a plateau from $Pt_{10}Sn_3O_6$ (−290 kJ/mol) to $Pt_{10}Sn_3O_{14}$ (−272 kJ/mol) and finally increases further by coadsorbing more O atoms. In general, the O adsorption energy on supported $Pt_{10}Sn_3$ cluster is weaker (by almost 25%) than that on supported Pt_{13} cluster[12] (Figure 2). In comparison with the Pt_3Sn (111) surface,[24] the supported $Pt_{10}Sn_3$ cluster exhibits stronger adsorption energy which shows a huge capacity of stabilizing oxygen atoms on it. This is due to the intrinsic metastability of such small size clusters with respect to infinite surface, and also to the capacity of these small clusters to adapt their shape upon adsorption, a consequence of their ductility, as previously shown for H adsorption on Pt[40,41] and PtSn clusters.[19] Notably, starting from $n = 10$, the structure of the

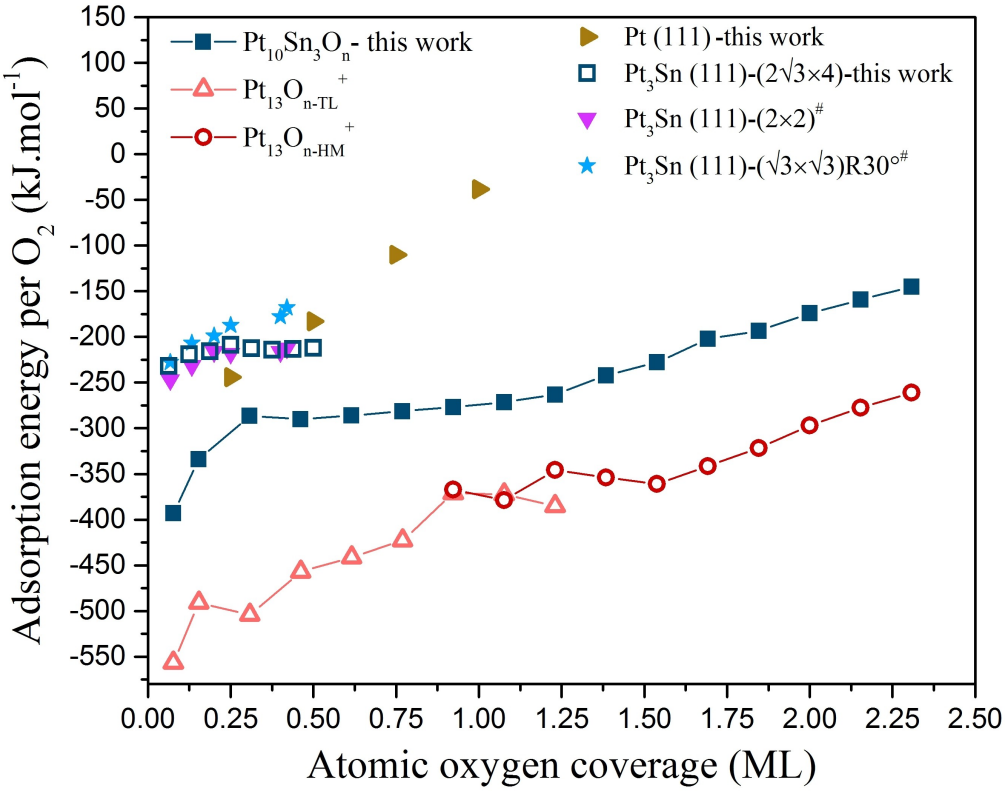

Figure 2. Average adsorption energy (kJ mol^{-1}) plotted against oxygen coverage (ML) on $Pt_{10}Sn_3/Al_2O_3$. The calculated adsorption energies of oxygen on Pt (111), Pt_3Sn (111) and Pt_{13}/Al_2O_3 are also presented from previous works: $^{+}$Sangnier *et al.*[12] and $^{\#}$Dupont *et al.*[24] The reported adsorption energies taken from Ref. [24] which were expressed per atomic oxygen, are therefore multiplied by a factor two to be compared with other values.

support is locally affected, with the migration of a surface Al atom to a neighboring Al_{IV} position close to the surface.

Structural and electronic properties

To investigate the impact of the metal/support interaction on the structure, the averaged Pt–Al, Pt–O, Pt–Pt, Pt–Sn and Sn–O bond lengths are plotted against oxygen coverage in Figure 3. The Pt–Al bond length slightly increases from 2.70 Å for the uncovered cluster to 2.90 Å for the highest oxygen coverage, in line with the uplift of the cluster. The Pt–Pt bond length in the cluster increases for increasing O coverages from 2.85 Å for $n=0$ to 3.45 Å for $n=30$, exceeding the Pt–Pt bond length in the PtO_2 bulk phase. This is due to the intercalation of oxygen in Pt–Pt bonds. The Pt–O bond length for $n=16$ and 18 is close to Pt–O bond length of bulk PtO. The Pt–Sn bond length for lower O coverages is close to its value in the Pt_3Sn bulk structure (~ 2.80 Å), while it dramatically increases to 3.45 Å for $n=16$ and then slightly decreases to 3.20 Å for the highest oxygen coverage. This results from the formation of a Sn-oxide entities leading to a segregation of Sn and Pt in their respective oxide entities. The Pt–O bond length is very weakly sensitive to O coverage increase (between 2.10 Å and 2.00 Å), quite close to Pt–O bond length in bulk PtO and PtO_2.

The Sn–O bond length first decreases from 2.30 Å for $n=2$ to 2.10 Å for $n=10$ and then reaches a plateau from $n=12$ to $n=20$ and then decreases again by adsorbing more O atoms to reach 1.90 Å for the highest coverage. The Sn–O bond length for $n=2$, 12, 14, 16, 18 and 20 is quite close to Sn–O bond length of bulk SnO while it reaches the Sn–O bond length of bulk SnO_2 for n between 4 and 10 but also for $n>26$. Hence, although the number Sn atoms is more than 3 times lower than the number of Pt atoms in the cluster, Sn and O atoms interact with each other whatever the coverage of O atoms. To a certain extent, this trend can be qualitatively compared with the stronger affinity of Ag atoms with O in Ag_9Pt_2 cluster supported on α-alumina during CO oxidation reaction.[17] The averaged Sn–Sn distance non-monotonically decreases from 3.67 Å for the uncovered cluster to 3.32 Å for the highest oxygen coverage (Figure 3) which shows Sn atoms slightly segregated in Sn-oxide entities by increasing the number of O atoms. Interestingly, a similar shortening of the Sn–Sn bond length is observed between when moving from SnO and to SnO_2 bulk phases. The presence of sufficient O atoms induces the formation monomeric or dimeric entities as can be found in SnO or SnO_2 materials. For instance, for $n>10$, a dimeric diamond Sn-O–Sn-O unit is formed and stabilized at the top of the $Pt_{10}Sn_3O_n$ clusters (Figure S3).

Figure 4 illustrates the evolution of the interaction energy between the alumina support and the oxidized $Pt_{10}Sn_3$ clusters

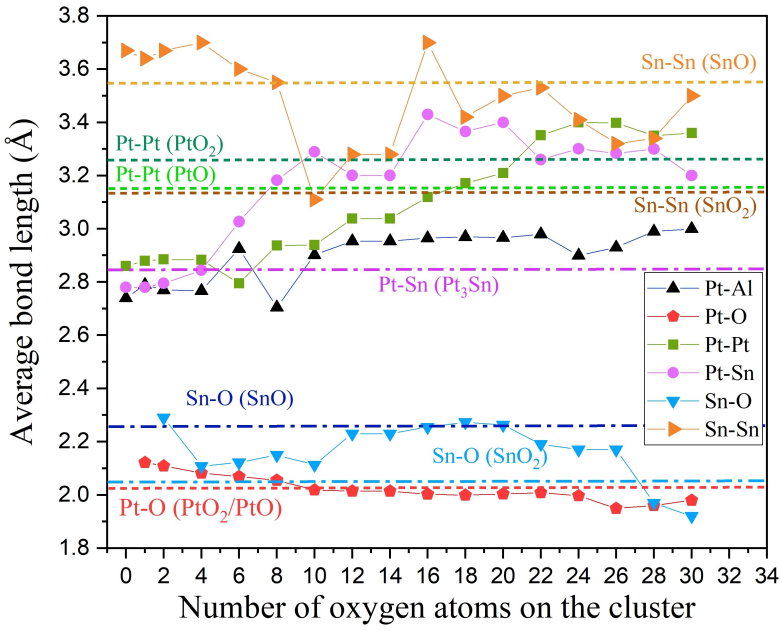

Figure 3. Averaged Pt–Al, Pt–O Pt–Pt, Pt–Sn, Sn–O and Sn–Sn bond lengths (Å) as a function of the number of adsorbed oxygen atoms. The maximal bond lengths were set to 3.0 Å for Pt–Al, 2.5 Å for Pt–O, 3.8 Å for Pt–Pt, 3.8 Å for Pt–Sn and 2.5 Å for Sn–O. Dotted red, dotted dark green, dash dotted light blue and dash dotted purple lines correspond to the Pt–O, Pt–Pt, Sn–O and Pt–Sn bond lengths in PtO_2 and SnO_2 bulk phases, respectively. Dotted light green, dotted red, dash dotted dark blue lines correspond to the Pt–Pt, Pt–O and Sn–O bond lengths in PtO and SnO bulk phases, respectively.

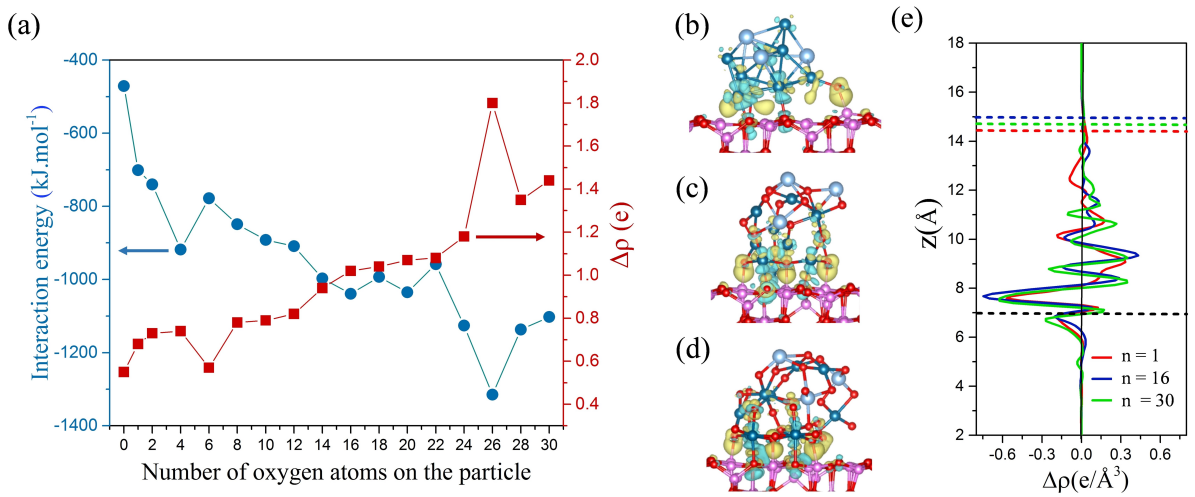

Figure 4. (a) Evolution of the interaction energy between the alumina support and the oxidized platinum-tin clusters and the Bader charge transfer from alumina surface to $Pt_{10}Sn_3O_n$ cluster). (b) Charge density difference $\Delta\rho = \rho\ (Pt_{10}Sn_3O_n/\gamma\text{-}Al_2O_3) - \rho\ (\gamma\text{-}Al_2O_3) - \rho\ (Pt_{10}Sn_3O_n)$ for n = 1 (b), n = 16 (c) and n = 30 (d). $\Delta\rho$ is illustrated by iso-surfaces bounding regions of electron accumulation at +0.007 e/Å^3 (yellow) and electron depletion at −0.007 e/Å^3 (cyan). (e) planar-averaged charge density difference $\langle\Delta\rho(z)\rangle$ for x = 1, 16 and 30. The dashed black line shows the position of the topmost Al_2O_3 surface layer, the dashed red, blue and green lines indicate the position of the topmost metallic atom in the cluster for structures with 1, 16 and 30 O atoms, respectively. Positive $\Delta\rho(z)$ means that the cluster has gained some electrons. Color code as in Figure 1.

and the Bader charge transfer (from the alumina surface to the $Pt_{10}Sn_3O_n$ cluster). These results show that the interaction energy between the oxidized platinum-tin cluster and the alumina support globally strengthens as the oxygen coverage increases. This trend is similar to the one observed for Pt_{13} cluster supported on alumina (100) surface[12] although it is much more pronounced in the present case. This may be due to a stronger electrostatic metal-oxygen (from the support) interaction as Sn is more positively charged than Pt (see Figure 5). By contrast, this trend is opposite to the one reported upon hydrogen coverage increase.[19] Similarly, the Bader charge transfer from the alumina surface to the $Pt_{10}Sn_3O_n$ cluster enhances with increasing O coverage. The irregular point at n = 26 can be explained by the existence of a O=O bond involving one O atom from the support, that is strongly oxidized with respect to other oxygen atoms from the alumina surface. The

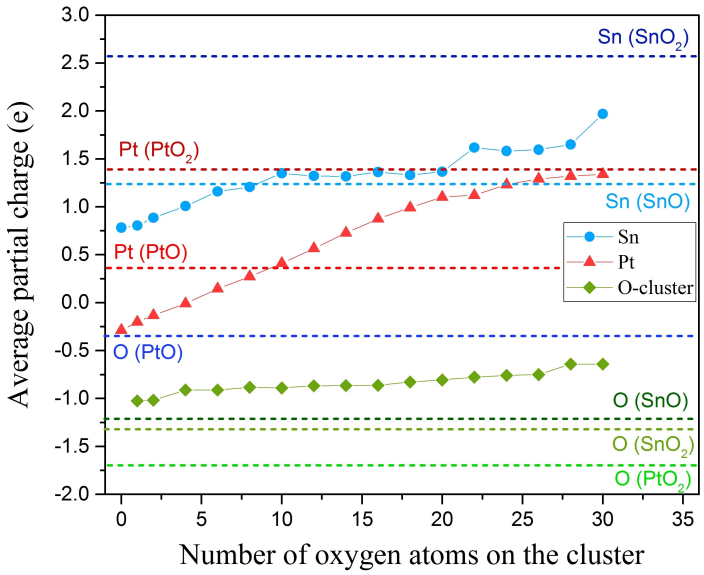

Figure 5. Average Bader charge (in electron) per Pt (red), cluster O (green), surface O (orange), Sn (blue) and Al (purple) atoms as a function of the number of adsorbed oxygen atoms. Dotted lines correspond to the average Bader charge of O, Pt and Sn atoms in the bulk structures of PtO_2, PtO, SnO_2 and SnO.

charge density difference (Figure 4 b-e) shows that two large peaks of electron depletion are present at the interface between the cluster and alumina increases, whereas charge accumulation is more predominant in the cluster (far above the interface) and is enhanced with increasing O coverage.

To highlight more clearly the impact of oxygen coverage on charge transfer, the Bader partial charges were computed for each atom in the $Pt_{10}Sn_3O_n/Al_2O_3$ systems (Figure 5). The charge of oxygen atoms in the metallic cluster slightly increases (between −1 and −0.6 e) as the O coverage increases. The charge of platinum increases almost linearly with coverage, starting from −0.25 e for the uncovered cluster to a 1.3 electron-depleted platinum for $Pt_{10}Sn_3O_{30}$ cluster, quite close to a kind of bulk PtO_2 charge. A similar trend was found for the $Pt_{13}O_n$ cluster on alumina.[12] Interestingly for n = 10 (O/Pt = 1), the partial charge of Pt is very close to the one of Pt in PtO bulk. The charge of Sn atoms first increases from 0.75 e for uncovered cluster to 1.3 e for $n = 10$ and then reaches a plateau between $n = 10$ and $n = 20$, quite close to the Sn charge in bulk SnO, and then increases by adsorbing more O atoms approaching to the bulk SnO_2 charge (2.51 e). For the uncovered cluster, a Sn to Pt electron transfer occurs as already discussed in Ref. [19]. Then, Sn atoms are always more positively charged that Pt, but the difference decreases while increasing the oxygen coverage above n = 10. This illustrates the gradual oxidation of both metals, but mainly Pt is oxidized for n > 10. The total charge of the cluster (not shown) gradually increases with the oxygen coverage, but more smoothly than the charge of the individual elements, from −0.50 within oxygen, to 0.2 at n = 30.

Thermodynamic diagrams

We first compare the reference cases of Pt(111) and $Pt_3Sn(111)$ surfaces (Figure S4 and 6 a, respectively). Due to similar energetics of O atoms on Pt(111) and on $Pt_3Sn(111)$ as highlighted in Figure 2, these diagrams are dominated by 0.00, 0.25 and 0.50 ML. At high temperature and low pressure, it is thermodynamically not favorable for oxygen atoms to remain adsorbed on the $Pt_3Sn(111)$ and Pt(111) surfaces. By increasing pressure and decreasing temperature, two main domains are stabilized with 0.25 ML and 0.5 ML coverage on both surfaces. On $Pt_3Sn(111)$, at 10^{-6} bar, the 0.25 ML O ad-atom phase is stable over the interval of temperature of ~625 K and ~750 K, while 0.5 ML is stabilized for T < ~625 K. By contrast, the 0.5 ML domain vanishes for T > ~375 K on Pt(111) (Figure S4). As a consequence, the 0.50 ML domain is wider on $Pt_3Sn(111)$ due to the higher adsorption energies of O atoms for this coverage on $Pt_3Sn(111)$ than on Pt(111) (Figure 2). Two very thin domains of stability are also observed on the $Pt_3Sn(111)$ diagram at 0.06 ML and 0.38 ML.

The (p_{O_2}, T) phase diagram for $Pt_{10}Sn_3O_n/Al_2O_3$ (100) within the pressure range from 1×10^{-16} to 1×10 bar and the temperature range 0 to 1000 K is shown in Figure 6 b. The equivalent thermodynamic phase diagram for the most stable oxygen coverage on Pt_{13}/Al_2O_3 (100) from the previous published data by Sangnier *et al.*[12] is recalled in Figure S6. As for Pt_{13}/Al_2O_3 (100) system, the phase diagram of the supported $Pt_{10}Sn_3$ cluster shows a large diversity of stable O contents, revealing a smoother transition from zero coverage to 1.85 ML. This diversity is not observed for the ideal Pt(111) and Pt_3Sn (111) surfaces (Figure S4 and 6b) which reflects that the clusters exhibit more numerous types of sites subject to many reconstructions. Indeed, the clusters are ductile enough to accommodate many O-contents upon reconstruction contrast-

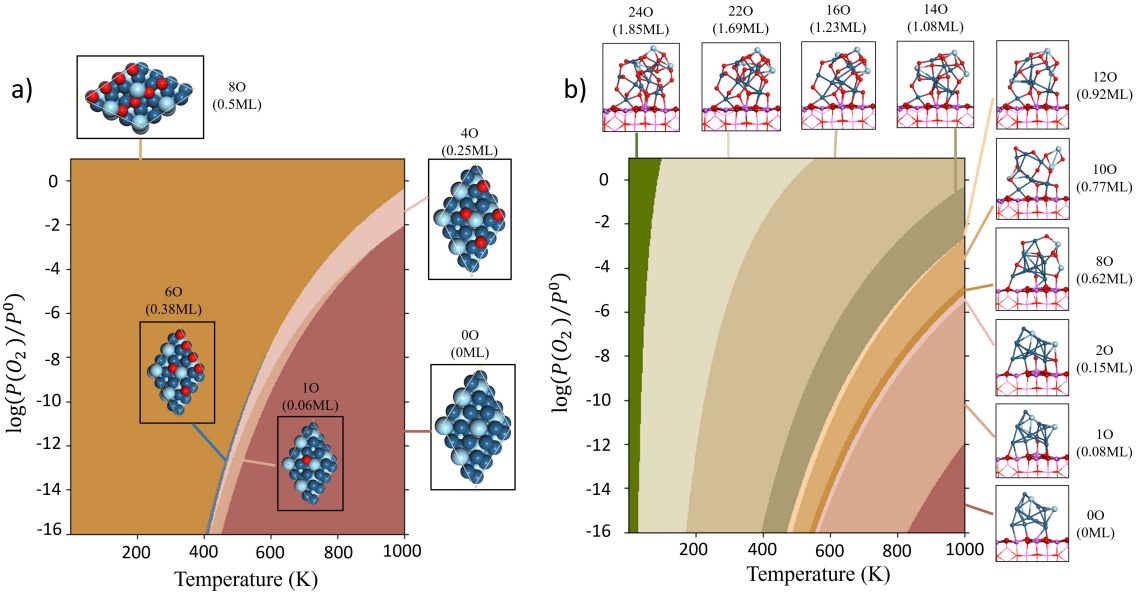

Figure 6. Thermodynamic phase diagrams depicting the most stable oxygen coverages as a function of temperature (K) and the O_2 partial pressure (bar) for a) Pt_3Sn (111) and b) $Pt_{10}Sn_3/Al_2O_3$ (100). The structures of the systems exhibiting a significant stability domain are also depicted with top views for a) and side views for b). Color code for the atomic structures is the same as in Figure 1.

ing with the more rigid surfaces. This ductility of clusters was highlighted by our structural analysis showing large expansion of the mean Pt–Pt (~0.5 Å) and Pt–Sn (~0.6 Å) bond lengths inside the cluster as a function of O coverage. This massive structural expansion is not possible on the surface, even though Sn buckling is observed at high oxygen coverage on the later (above 0.32 ML). Moreover, as discussed in a previous study,[42] the binding energy of Pt_n clusters decrease as a function of n, which reflects the higher metastability of such small size's cluster with respect to larger ones represented by ideal surface. Hence, the intrinsic reactivity of the cluster is expected to be higher and its affinity for O atoms to be greater, which is consistent also with earlier DFT study on gas phase Pt cluster.[11]

The system at zero oxygen coverage is stable at very low pressure ($<10^{-12}$ bar) for temperature greater than 800 K for $Pt_{10}Sn_3/Al_2O_3(100)$ and 900 K for $Pt_{13}/Al_2O_3(100)$, contrasting with Pt(111) and Pt_3Sn (111) surfaces, where 0 ML appears already above ~525–550 K. Hence, contrary to the cases of Pt(111) and $Pt_3Sn(111)$ surfaces, both supported $Pt_{10}Sn_3$ and Pt_{13} clusters are thus oxidized (0.08 ML) as soon as a very weak oxygen partial pressure (above 10^{-12} bar) is applied on the medium (in the absence of reducing agent). As explained before, the stabilization of the first and second O atom added to the system is induced by the presence of the interface between the alumina surface and the cluster itself. At this early oxidation stage, such a phenomenon is thus not induced by the ductility of the cluster (the corresponding clusters exhibit rather similar structures for 0, 1 or 2 oxygen atoms) but rather by the greater reactivity of interfacial sites. This trend is enhanced in the case of ultra-dispersed sub-nanometric clusters such as $Pt_{10}Sn_3$ and Pt_{13} with large proportion of interfacial atoms, whereas it is expected to be less predominant for larger metallic particles even supported on alumina. Interestingly, the role of such interfacial O-atoms for CO oxidation has been addressed in the case of Pt cluster supported on reducible oxide.[7] Here, due to the low reducibility character of alumina, O atoms coming from the gas phase O_2 dissociation are stabilized at the Pt/alumina interface.

Sn-doping supported of the Pt cluster slightly shifts the desorption frontiers to lower temperatures and lower O partial pressures except for the transitions from n = 14 to 8 oxygen atoms, corresponding to the adsorption energy plateau observed in Figure 2, for coverages between 0.62 (n = 8) and 1.08 (n = 14). This slight stabilizing effect of the $Pt_{10}Sn_3O_{n=8\text{-}14}$ structures might be induced by the presence of sufficient O atoms to favor the formation of monomeric or dimeric entities as can be found in SnO or SnO_2 materials. As aforementioned, the $Pt_{10}Sn_3O_{n=10\text{-}14}$ clusters reveals the formation of diamond Sn-O–Sn-O unit capping the Pt cluster. In spite of this small discrepancy, for wide reaction conditions of 300–1000 K and 10^{-6}–1 bar, the two systems are crossing very similar domains of oxygen coverages: $Pt_{10}Sn_3O_n/Al_2O_3$ is occupied by 2–20 oxygen atoms, while Pt_{13}/Al_2O_3 is covered by 4–20 atoms. Compared with the $Pt_3Sn(111)$ surface, the supported $Pt_{10}Sn_3$ system reaches much higher O coverages in similar conditions, illustrating a strong size effect enhancing the interaction of oxygen with small alloyed clusters. In addition to lower coordination numbers of Pt and Sn atoms in the cluster, this trend is due to the very strong deformation ability of the cluster, stronger than that of the surface. This ductility of the cluster is associated to its significant metastability with respect to big alloyed metallic particles represented by ideal surface in the present study. From a more fundamental aspect, it would be interesting in a future study to compare the behavior of

alumina supported $Pt_{10}Sn_3$ clusters with the case of gas phase $Pt_{10}Sn_3$ clusters in order to finely disentangle the role of the support and the size effect per se.

Conclusion

By using periodic DFT calculations and AIMD simulations, we investigated oxygen adsorption on γ-Al_2O_3 supported $Pt_{10}Sn_3$ cluster and systematically compared them with pure Pt_{13} cluster, Pt_3Sn(111) and Pt(111) surfaces. According to DFT calculations, the interfacial alumina/Pt sites are the preferred sites for the adsorption of the first two O atoms on the supported $Pt_{10}Sn_3$ cluster. This interfacial effect occurring on both alloyed $Pt_{10}Sn_3$ and pure Pt_{13} clusters is the first one enhancing the oxidation level of supported cluster with respect to large metallic (alloyed or non-alloyed) particles represented by the Pt_3Sn(111) and Pt(111) surfaces.

In addition, we showed that the morphology of metallic cluster drastically changes for more than one O_2 molecule dissociated on the cluster. The oxygen adsorption energies on supported $Pt_{10}Sn_3$ are thus significantly stronger from that obtained for the Pt_3Sn(111) flat surface, which indicates a huge capacity of stabilizing oxygen atoms on it, as a consequence of the size of the cluster at the origin its significant ductility and intrinsic metastability. This ductility effect was carefully characterized by the analysis of Pt–Pt, Pt–Sn, Pt–O and Sn–O bond lengths evolution as well as Bader charge redistribution inside the whole system as a function of O coverages.

Nevertheless, although the adsorption energies on $Pt_{10}Sn_3$/γ-Al_2O_3 system are weaker (by 25–30%) than those on Pt_{13}/γ-Al_2O_3 system, the temperature-pressure phase diagram obtained from ab initio thermodynamic data revealed only minor qualitative differences between pure Pt_{13} cluster and $Pt_{10}Sn_3$. This counter-intuitive trend results from the very strong interactions of O atoms with both clusters which are thus covered by O atoms also at high T and low P. For Pt_3Sn(111) and Pt(111) surfaces, the thermodynamic diagrams depend also weakly on the presence of Sn, but their oxidation level is significantly weaker due to reduced adsorption energies (by up to ~50%) with respect to clusters. As a consequence, the main effect driving oxidation is the size effect and not the alloying effect.

Hopefully, this work opens the door to a better understanding of the reactivity of alloyed sub-nanometric clusters in oxidative conditions, that are widespread in heterogeneous catalysis.

Computational details

DFT calculations with periodic boundary conditions were performed by using the Vienna Ab initio Simulation Package (VASP)[43] with the generalized gradient approximation Perdew – Burke – Ernzerhof exchange correlation functional.[44] A kinetic cut-off energy of 400 eV was used for the expansion of the plane waves, while core electrons were described with the projected augmented wave method (PAW).[45] The total electronic energy convergence criterion was set to 10^{-6} eV and all geometries were optimized until forces on atoms allowed to relax were lower than 0.02 eV/Å. A Gaussian smearing with $\sigma = 0.02$ eV was used for the supported $Pt_{10}Sn_3O_n$ clusters. The charge transfer was estimated *via* the Bader charge analysis[46] at the same level of theory.

The model of the $Pt_{10}Sn_3$ cluster supported on the γ-Al_2O_3(100) dehydrated surface was described previously in detail[19] (Figure S1). It was built on the basis of the γ-Al_2O_3(100) surface model by Digne *et al.*,[47] that is dehydrated in a large range of relevant operating conditions (concerning temperature and water partial pressure). The dimensions of the cells are $16.71 \times 16.79 \times 25.80$ Å^3 in which the thickness of γ-Al_2O_3 slab is 7.2 Å along z-axis and each periodically equivalent slab is separated by a sufficient vacuum space of 15 Å. For all calculations, a dipolar correction was added to the total electronic energy in the direction perpendicular to the slabs. Sampling of the Brillouin zones was performed by using the Monkhorst-Pack[48] approach at the Γ point for the study of these systems. In all geometry optimizations and ab initio molecular dynamics simulations, the two topmost alumina layers were fully relaxed, as well as all atoms in the cluster, whereas the two alumina bottom layers were frozen (Figure S1).

For PtSn clusters covered by several oxygen atoms, the average coadsorption energy per O_2 molecule is defined using the following equation related to the simultaneous dissociative adsorptions of several dioxygen molecules (equation (1)):

$$E_{ads} = \frac{2}{n}\left[E_{Pt_{10}Sn_3O_n/Al_2O_3} - E_{Pt_{10}Sn_3/Al_2O_3} - \frac{n}{2}\,E_{O_2}\right] \quad (1)$$

Corresponding to the chemical equation given in equation (2):

$$Pt_{10}Sn_3/Al_2O_3 + \frac{n}{2}O_2 = Pt_{10}Sn_3O_n/Al_2O_3 \quad (2)$$

where n is the number of oxygen atoms adsorbed per cell on $Pt_{10}Sn_3$/γ-Al_2O_3 system and $E_{Pt_{10}Sn_3O_n/Al_2O_3}$ and $E_{Pt_{10}Sn_3/Al_2O_3}$ are the total electronic energies of the system considered with or without adsorbed oxygen, respectively. The energy of O_2 (E_{O_2}) was calculated by placing a O_2 molecule into an asymmetric $15 \times 16 \times 17$ Å^3 box and by performing spin polarized calculations.

For $n > 1$, the most stable structure for each O coverage was determined first by optimizing different adsorption geometries (static calculations), and second by equilibrating these optimized structures with velocity-scaled AIMD at 600 K, with a time-step of 5 fs over 1200 steps. The AIMD tool was thus used in an explorative mode to sample the configurational space. For some oxygen coverages ($n = 4$, 14, and 24), the AIMD trajectories were extended up to 2000 steps. As illustrated in Figure S2, competitive structures were extracted from the AIMD simulations at the lowest potential energy and quenched at 0 K by performing standard geometry optimizations with the same parameters as previously detailed. We used the most stable quenched geometries obtained after AIMD simulations to predict the thermodynamic diagram as detailed in Ref. [12]. Such an approach combining velocity-scaled MD, quenching followed by thermodynamic calculations in the harmonic approximation has been found to be efficient and robust in the case of platinum and platinum-tin clusters supported on alumina, with a variety of adsorbates.[4,12,19,40,49]

The interaction energy between the support and the platinum-tin cluster was calculated using equation (3):

$$E_{interaction} = E_{Pt_{10}Sn_3O_n/\gamma-Al_2O_3} - E^*_{Pt_{10}Sn_3O_{2n}} - E^*_{\gamma-Al_2O_3} \quad (3)$$

where and $E^{*}_{Pt_{10}Sn_3O_n/\gamma-Al_2O_3}$ is the total electronic energy of supported systems from geometry optimization calculations and $E^{*}_{Pt_{10}Sn_3O_n}$ and $E^{*}_{\gamma-Al_2O_3}$ are the total electronic energies with single point calculations for the separate cluster and support systems at the geometry of the supported system. This energy refers to chemical bonding in absence of deformation energies of separate partners.

The Pt(111) and Pt_3Sn (111) surfaces were modeled with $p(2\times2)$ and $p(2\sqrt{3}\times4)$ supercells and periodic slabs consisting of five atomic layers, respectively, where the three bottom metallic planes were frozen and the two top layers were fully relaxed. Gamma-centered $6\times6\times1$ and $4\times4\times1$ k-point grids were chosen for the Pt(111) and Pt_3Sn(111) surfaces, respectively. The optimized lattice parameters and corresponding k-point grids for Pt, Pt_3Sn PtO, PtO_2, SnO and SnO_2 bulk structures are presented in Table S1.

To build the (p_{O_2}, T) phase diagram, the adsorption entropies and enthalpies are obtained by using DFT optimized structures and corresponding harmonic frequency calculations. The harmonic vibrational analysis was performed on the most stable structure obtained for each coverage with a displacement of ±0.01 Å in each direction for all relaxed atoms in the cell. The Hessian matrix was then calculated by the finite-difference method and diagonalized to predict harmonic normal modes and associated vibrations. For the condensed phases, 3N-3 real vibrational frequencies were considered to evaluate the thermal and entropy contributions. Free energy calculations for each system are detailed in the Supporting Information S5. To build the thermodynamic diagrams, we used the oxygen-adsorption free energy $\Delta G_{adsorption}$ which is given in Equation 4. The coverage domains represented on the various thermodynamic diagrams correspond to the lowest free energy values obtained at (p_{O_2}, T) according to:

$$\Delta G_{adsorption}\left(p_{O_2}, T, \theta_{O_2}\right) = G_{Pt_{10}Sn_3O_n}\left(T, \theta_{O_2}\right) - G_{Pt_{10}Sn_3}(T) - \frac{n}{2}G_{O_2}(p_{O_2}, T) \quad (4)$$

Acknowledgements

This work is part of the "RatiOnAl Design for CATalysis" (ROAD4-CAT) industrial chair, project IDEXLYON funded by the French National Research Agency (ANR-16-IDEX-0005) and the Commissariat-General for Investment (CGI) within the framework of Investissements d'Avenir program ("Investment for the future"). Calculations were performed using HPC resources from GENCI-CINES (Grant A0020806134) and from IFP Energies nouvelles (ENER440). The authors thank PSMN (Data Center) in Lyon for CPU time and assistance, the CPER/SYSPROD 2015–2022 project (N°2019-AURA-P5B).

Conflict of Interest

The authors declare no conflict of interest.

Data Availability Statement

The data that support the findings of this study are available from the corresponding author upon reasonable request.

Keywords: Alloys · DFT calculation · clusters · oxygen adsorption · size effect

[1] A. N. Jahel, V. Moizan-Basle, C. Chizallet, P. Raybaud, J. Olivier-Fourcade, J.-C. Jumas, P. Avenier, S. Lacombe, *J. Phys. Chem. C* **2012**, *116*, 10073–10083.
[2] a) P. Avenier, et al., *Oil & Gas Sci. Technol. – Revue IFP Energies Nouvelles* **2016**, *71*, 41; b) P.-Y. Le Goff, W. Kostka, J. Ross, *18. Catalytic Reforming*, in Springer Handbook of Petroleum Technology. pp 589–616, Eds: P. R. Robinson, C. S. Hsu. Springer International Publishing, **2017**; c) J. H. Sinfelt, *Catalytic Reforming*, in Wiley-VCH Verlagsgesellschaft mbH. pp 1939–1955, Eds: G. Ertl, E. Knözinger, J. Weitkamp, Weinheim, **1997**.
[3] a) J. Sattler, J. Ruiz-Martinez, E. Santillan-Jimenez, B. M. Weckhuysen, *Chem. Rev.* **2014**, *114*, 10613–10653; b) J. Zhu, M.-L. Yang, Y. Yu, Y.-A. Zhu, Z.-J. Sui, X.-G. Zhou, A. Holmen, D. Chen, *ACS Catal.* **2015**, *5*, 6310–6319; c) C. Wang, D. Astruc, *Chem. Soc. Rev.* **2021**, *50*, 3437–3484; d) Y. Sekine, T. Higo, *Top. Catal.* **2021**, *64*, 470–480.
[4] W. Zhao, C. Chizallet, P. Sautet, P. Raybaud, *J. Catal.* **2019**, *370*, 118–129.
[5] a) S. H. Oh, P. J. Mitchell, R. M. Siewert, *J. Catal.* **1991**, *132*, 287–301; b) E. Becker, P.-A. Carlsson, H. Grönbeck, M. Skoglundh, *J. Catal.* **2007**, *252*, 11–17; c) K. Otto, J. M. Andino, C. L. Parks, *J. Catal.* **1991**, *131*, 243–251.
[6] a) J. A. Anderson, *J. Chem. Soc. Faraday Trans.* **1992**, *88*, 1197–1201; b) Y.-F. Y. Yao, *J. Catal.* **1984**, *87*, 152–162.
[7] S. Kaiser, F. Maleki, K. Zhang, W. Harbich, U. Heiz, S. Tosoni, B. A. J. Lechner, G. Pacchioni, F. Esch, *ACS Catal.* **2021**, *11*, 9519–9529.
[8] a) F. V. Hanson, M. Boudart, *J. Catal.* **1978**, *53*, 56–67; b) M. Nesselberger, M. Roefzaad, R. F. Hamou, P. U. Biedermann, F. F. Schweinberger, S. Kunz, K. Schloegl, G. K. H. Wiberg, S. Ashton, U. Heiz, K. J. J. Mayrhofer, M. Arenz, *Nat. Mater.* **2013**, *12*, 919–924.
[9] T. Kim, Y. Song, J. Kang, S. K. Kim, S. Kim, *Int. J. Hydrogen Energy* **2022**, *47*, 24817–24834.
[10] J. Singh, E. M. C. Alayon, M. Tromp, O. V. Safonova, P. Glatzel, M. Nachtegaal, R. Frahm, J. A. van Bokhoven, *Angew. Chem. Int. Ed.* **2008**, *47*, 9260–9264; *Angew. Chem.* **2008**, *120*, 9400–9404.
[11] Y. Xu, W. A. Shelton, W. F. Schneider, *J. Phys. Chem. A* **2006**, *110*, 5839–5846.
[12] A. Sangnier, M. Matrat, A. Nicolle, C. Dujardin, C. Chizallet, *J. Phys. Chem. C* **2018**, *122*, 26974–26986.
[13] a) L. G. Cesar, C. Yang, Z. Lu, Y. Ren, G. Zhang, J. T. Miller, *ACS Catal.* **2019**, *9*, 5231–5244; b) G.-Q. Ren, G.-X. Pei, Y.-J. Ren, K.-P. Liu, Z.-Q. Chen, J.-Y. Yang, Y. Su, X.-Y. Liu, W.-Z. Li, T. Zhang, *J. Catal.* **2018**, *366*, 115–126; c) S. Kobayashi, S. Kaneko, M. Ohshima, H. Kurokawa, H. Miura, *Appl. Catal. A* **2012**, *417–418*, 306–312; d) S. Rimaz, L. Chen, S. Kawi, A. Borgna, *Appl. Catal. A* **2019**, *588*, 117266; e) G. Wang, K. Lu, C. Yin, F. Meng, Q. Zhang, X. Yan, L. Bing, F. Wang, D. Han, *Catalysts* **2020**, *10*, 1042.
[14] T. Wang, F. Jiang, G. Liu, L. Zeng, Z. Zhao, J. Gong, *AIChE J.* **2016**, *62*, 4365–4376.
[15] L. Nykänen, K. Honkala, *ACS Catal.* **2013**, *3*, 3026–3030.
[16] T. J. Gorey, B. Zandkarimi, G. Li, E. T. Baxter, A. N. Alexandrova, S. L. Anderson, *ACS Catal.* **2020**, *10*, 4543–4558.
[17] F. R. Negreiros, et al., *Angew. Chem. Int. Ed.* **2018**, *57*, 1209–1213; *Angew. Chem.* **2018**, *130*, 1223–1227.
[18] a) W. M. H. Sachtler, *Catal. Rev.* **1976**, *14*, 193–210; b) G. A. Martin, *Catal. Rev.* **1988**, *30*, 519–562; c) J. H. Sinfelt, *Acc. Chem. Res.* **1977**, *10*, 15–20; d) R. Burch, *Acc. Chem. Res.* **1982**, *15*, 24–31; e) D. Uzio, G. Berhault, *Catal. Rev.* **2010**, *52*, 106–131; f) V. Ponec in *Advances in Catalysis* (Eds.: D. D. Eley, H. Pines, P. B. Weisz), Academic Press, **1983**; g) J. K. A. Clarke, A. C. M. Creaner, *Ind. Eng. Chem. Res.* **1981**, *20*, 574–593; h) W. Sachtler, R. A. van Santen in *Adv. Catal.* (Eds.: D. D. Eley, H. Pines, P. B. Weisz), Academic Press, **1977**.
[19] A. Gorczyca, P. Raybaud, V. Moizan, Y. Joly, C. Chizallet, *ChemCatChem* **2019**, *11*, 3941–3951.
[20] a) O. A. Bariås, A. Holmen, E. A. Blekkan, *Catal. Today* **1995**, *24*, 361–364; b) N. Kaylor, R. J. Davis, *J. Catal.* **2018**, *367*, 181–193.
[21] A. Iglesias-Juez, A. M. Beale, K. Maaijen, T. C. Weng, P. Glatzel, B. M. Weckhuysen, *J. Catal.* **2010**, *276*, 268–279.
[22] a) L. Nykänen, K. Honkala, *J. Phys. Chem. C* **2011**, *115*, 9578–9586; b) T. Srisakwattana, K. Suriye, P. Praserthdam, J. Panpranot, *Catal. Today* **2020**, *358*, 90–99.
[23] a) Z. Liu, G. S. Jackson, B. W. Eichhorn, *Angew. Chem. Int. Ed.* **2010**, *49*, 3173–3176; *Angew. Chem.* **2010**, *122*, 3241–3244; b) J. Parrondo, F. Mijangos, B. Rambabu, *J. Power Sources* **2010**, *195*, 3977–3983; c) S.

Knani, L. Chirchi, S. Baranton, T. W. Napporn, J.-M. Léger, A. Ghorbel, *Int. J. Hydrogen Energy* **2014**, *39*, 9070–9079.
[24] C. Dupont, Y. Jugnet, F. Delbecq, D. Loffreda, *J. Chem. Phys.* **2009**, *130*, 124716.
[25] R. M. Watwe, R. D. Cortright, M. Mavrikakis, J. K. Nørskov, J. A. Dumesic, *J. Chem. Phys.* **2001**, *114*, 4663–4668.
[26] a) J. Chen, G. Qian, B. Chu, Z. Jiang, K. Tan, L. Luo, B. Li, S. Yin, *Small* **2022**, *18*, 2106773; b) R. M. Mensharapov, N. A. Ivanova, D. D. Spasov, E. V. Kukueva, A. A. Zasypkina, E. A. Seregina, S. A. Grigoriev, V. N. Fateev, *Catalysts* **2021**, *11*, 1469.
[27] H. Huang, O. F. Blackman, V. Celorrio, A. E. Russell, *Electrochim. Acta* **2021**, *390*, 138811.
[28] X. Zhu, T. Wang, Z. Xu, Y. Yue, M. Lin, H. Zhu, *J. Energy Chem.* **2022**, *65*, 293–301.
[29] a) S. Deshpande, J. Greeley, *ACS Catal.* **2020**, *10*, 9320–9327; b) Z. Wang, Y. Chen, S. Mao, K. Wu, K. Zhang, Q. Li, Y. Wang, *Adv. Sustainable Syst.* **2020**, *4*, 2000092; c) T. J. Gorey, B. Zandkarimi, G. Li, E. T. Baxter, A. N. Alexandrova, S. L. Anderson, *J. Phys. Chem. C* **2019**, *123*, 16194–16209; d) H. Gao, *Chem. Phys. Lett.* **2016**, *657*, 11–17; e) H. Xu, M. Zhang, Y. Chen, H. Liu, K. Xu, X. Huang, *Comput. Theor. Chem.* **2015**, *1061*, 52–59.
[30] X. Wang, X. Li, S. Liao, B. Li, *Comput. Mater. Sci.* **2018**, *149*, 107–114.
[31] X. Huang, Y. Su, L. Sai, J. Zhao, V. Kumar, *J. Cluster Sci.* **2015**, *26*, 389–409.
[32] P. Euzen, P. Raybaud, X. Krokidis, H. Toulhoat, J.-L. Le Loarer, J.-P. Jolivet, C. Froidefond, *Alumina*, Wiley-VCH, Weinheim, in: F. Schüth, K. S. W. Sing, J. Weitkamp (Eds.) Handbook of Porous Solids, **2002**.
[33] a) A. T. F. Batista, W. Baaziz, A.-L. Taleb, J. Chaniot, M. Moreaud, C. Legens, A. Aguilar-Tapia, O. Proux, J.-L. Hazemann, F. Diehl, C. Chizallet, A.-S. Gay, O. Ersen, P. Raybaud, *ACS Catal.* **2020**, *10*, 4193–4204; b) A. T. F. Batista, C. Chizallet, F. Diehl, A.-L. Taleb, A.-S. Gay, O. Ersen, P. Raybaud, *Nanoscale* **2022**, *14*, 8753–8765.
[34] a) G. J. Siri, J. M. Ramallo-López, M. L. Casella, J. L. Fierro, F. G. Requejo, O. A. Ferretti, *Appl. Catal. A* **2005**, *278*, 239–249; b) M. Womes, F. Le Peltier, S. Morin, B. Didillon, J. Olivier-Fourcade, J. C. Jumas, *J. Mol. Catal. A* **2007**, *266*, 55–64.
[35] a) E. Fernández, M. Boronat, A. Corma, *J. Phys. Chem. C* **2015**, *119*, 19832–19846; b) P. Concepción, M. Boronat, S. García-García, E. Fernández, A. Corma, *ACS Catal.* **2017**, *7*, 3560–3568.
[36] P. Légaré, *Surf. Sci.* **2005**, *580*, 137–144.
[37] C. Dupont, Y. Jugnet, D. Loffreda, *J. Am. Chem. Soc.* **2006**, *128*, 9129–9136.
[38] R. F. de Morais, A. A. Franco, P. Sautet, D. Loffreda, *Phys. Chem. Chem. Phys.* **2015**, *17*, 11392–11400.
[39] R. M. Watwe, R. D. Cortright, M. Mavrikakis, J. K. Nørskov, J. A. Dumesic, *J. Chem. Phys.* **2001**, *114*, 4663–4668.
[40] C. Mager-Maury, G. Bonnard, C. Chizallet, P. Sautet, P. Raybaud, *ChemCatChem* **2011**, *3*, 200–207.
[41] E. Vottero, M. Carosso, A. Ricchebuono, M. Jiménez-Ruiz, R. Pellegrini, C. Chizallet, P. Raybaud, E. Groppo, A. Piovano, *ACS Catal.* **2022**, *12*, 5979–5989.
[42] C. Mager-Maury, C. Chizallet, P. Sautet, P. Raybaud, *ACS Catal.* **2012**, *2*, 1346–1357.
[43] a) G. Kresse, J. Furthmüller, *Phys. Rev. B* **1996**, *54*, 11169–11186; b) G. Kresse, J. Furthmüller, *Comput. Mater. Sci.* **1996**, *6*, 15–50.
[44] J. P. Perdew, K. Burke, M. Ernzerhof, *Phys. Rev. Lett.* **1996**, *77*, 3865–3868.
[45] G. Kresse, D. Joubert, *Phys. Rev. B* **1999**, *59*, 1758–1775.
[46] a) E. Sanville, S. D. Kenny, R. Smith, G. Henkelman, *J. Comput. Chem.* **2007**, *28*, 899–908; b) G. Henkelman, A. Arnaldsson, H. Jónsson, *Comput. Mater. Sci.* **2006**, *36*, 354–360.
[47] a) M. Digne, P. Sautet, P. Raybaud, P. Euzen, H. Toulhoat, *J. Catal.* **2002**, *211*, 1–5; b) M. Digne, P. Sautet, P. Raybaud, P. Euzen, H. Toulhoat, *J. Catal.* **2004**, *226*, 54–68.
[48] H. J. Monkhorst, J. D. Pack, *Phys. Rev. B* **1976**, *13*, 5188–5192.
[49] a) A. Gorczyca, V. Moizan, C. Chizallet, O. Proux, W. Del Net, E. Lahera, J.-L. Hazemann, P. Raybaud, Y. Joly, *Angew. Chem. Int. Ed.* **2014**, *53*, 12426–12429; *Angew. Chem.* **2014**, *126*, 12634–12637; b) A. Sangnier, E. Genty, M. Iachella, P. Sautet, P. Raybaud, M. Matrat, C. Dujardin, C. Chizallet, *ACS Catal.* **2021**, *11*, 13280–13293.

Manuscript received: September 5, 2022
Revised manuscript received: October 16, 2022
Accepted manuscript online: October 19, 2022
Version of record online: November 17, 2022